Elastic X-ray scattering from state-selected molecules

Elastic X-ray scattering from state-selected molecules

Thomas Northey,[1] Andrés Moreno Carrascosa,[1] Steffen Schäfer,[2] and Adam Kirrander[1, a)]

[1)] *EaStCHEM, School of Chemistry, University of Edinburgh, David Brewster Road, EH9 3FJ Edinburgh, UK*

[2)] *Aix-Marseille Université and Institut Matériaux Microélectronique Nanosciences de Provence (IM2NP), Marseille, France*

(Dated: 16 June 2016)

The characterization of electronic, vibrational and rotational states using elastic (coherent) X-ray scattering is considered. The scattering is calculated directly from complete active space self-consistent field (CAS-SCF) level *ab-initio* wavefunctions for H_2 molecules in the ground-state $X^1\Sigma_g^+$ and first-excited $EF^1\Sigma_g^+$ electronic states. The calculated scattering is compared to recent experimental measurements (Y.-W. Liu *et al.* Phys. Rev. A 89, 014502 (2014)), and the influence of vibrational and rotational states on the observed signal is examined. The scaling of the scattering calculations with basis set is quantified, and it is found that energy convergence of the *ab-initio* calculations is a good indicator of the quality of the scattering calculations.

[a)] Electronic mail: Adam.Kirrander@ed.ac.uk

I. INTRODUCTION

Ever since Bragg's original discovery in 1912, X-ray scattering has dramatically advanced our understanding of the structure of matter, ranging from atoms to proteins, crystals and solids. Despite the historical importance of gas-phase X-ray scattering[1–5], electron scattering came to dominate experiments in the gas-phase on account of the greater scattering cross-sections of electrons[6]. Now, however, rapid development of synchrotron sources, detectors, and new X-ray Free-Electron Lasers (XFELs)[7–12] has sparked renewed interest in gas-phase X-ray scattering[13–21].

Recent double differential, and hence energy-resolved, synchrotron-based measurements of X-ray scattering cross-sections[13–16] include the measurement of elastic X-ray scattering from gas-phase H_2 in the electronic ground-state[13]. Furthermore, the technology to orient and align molecules experimentally is developing rapidly[22–24]. For instance, Bartlett *et al.*[23] report retention of initial polarisation for >100 ns for $H_2(v = 1, J = 2, M = 0, 2)$ and in a recent experimental article, Mukherjee *et al.*[24] demonstrate population transfer of 73% using Stark-induced adiabatic Raman passage[25]. It therefore appears timely to consider probing of gas-phase molecules in specific vibrational, rotational, and electronic states by elastic X-ray scattering.

Theoretically the characterization of electronic states using elastic X-ray scattering has been considered previously[26–28], and metastable electronically excited states have been detected indirectly in experiments via changes in molecular geometry[29,30]. In the current article, we account not only for the electronic state of the molecules, but simultaneously account for the electronic, vibrational and rotational degrees of freedom, thus providing a complete state-specific characterization of the molecular states. The calculations are based on our recently developed *ab-initio* X-ray diffraction (AIXRD) method[28], which in this article is linked to vibrational and rotational motion, and are benchmarked against earlier calculations[31] and recent experiments[13]. In this context, it is worth mentioning related work on electron scattering that examined, separately, the theoretical signatures of vibrational[32] or rotational[33,34] states of molecules, with experimental results for partially aligned and state-selected molecules[35,36] demonstrating the potential of state-selective scattering. A related area is scattering from aligned molecules, which aims to minimize rotational averaging and thus enable measurement of scattering factors in the molecular frame. This has been considered theoretically[37–39] and realized experimentally using electrons[40] and X-rays[17].

II. THEORY

According to Fermi's golden rule, the total X-ray scattering cross section is[41],

$$\frac{dS}{d\Omega} = \left(\frac{d\sigma}{d\Omega}\right)_{\mathrm{Th}} \sum_n \left(\frac{\omega_n}{\omega_0}\right) \left|\langle\phi_n|\hat{L}\,|\phi_{\tilde{\alpha}}\rangle\right|^2, \tag{1}$$

where $(d\sigma/d\Omega)_{\mathrm{Th}} = \left(e^2/m_e c^2\right) K$ is the Thomson cross section of a free electron, with m_e and e the mass and charge of an electron, c the velocity of light, and K the polarization factor. The ω_n and ω_0 in Eq. (1) are the angular frequencies of scattered and incident X-rays, respectively, and ϕ_n and $\phi_{\tilde{\alpha}}$ are the final and initial states. The scattering operator is defined as,

$$\hat{L} = \sum_{j=1}^{N_{\mathrm{el}}} e^{\imath \mathbf{q}\mathbf{r}_j}, \tag{2}$$

where N_{el} is the number of electrons in the molecule, $\mathbf{r}_j$ the coordinates of each electron, and the momentum transfer vector, $\mathbf{q} = \mathbf{k}_0 - \mathbf{k}$, is defined as the difference between the incident and the scattered wave vectors, with $|\mathbf{k}| = |\mathbf{k}_0|$ for elastic scattering. Formally, the sum runs over all charged particles, but since particle mass appears in the denominator, only the electrons are included in Eq. (2) with the (e^2/m_e) factor incorporated into the Thomson cross section Eq. (1). Using completeness and ignoring the pre-factor (ω_n/ω_0), the total scattering given by Eq. (1) can be expressed in terms of the ground-state wavefunction and the relative position vectors of the electrons[42],

$$\frac{dS}{d\Omega} = \left(\frac{d\sigma}{d\Omega}\right)_{\mathrm{Th}} \langle\phi_{\tilde{\alpha}}| \sum_{i,j}^{N_{\mathrm{el}}} e^{\imath \mathbf{q}(\mathbf{r}_i - \mathbf{r}_j)} |\phi_{\tilde{\alpha}}\rangle, \tag{3}$$

which can further be expressed in terms of the electron-pair distribution function[43].

The diagonal, n=$\tilde{\alpha}$, term in the sum in Eq. (1) corresponds to the elastic (coherent) scattering that plays a key role in X-ray structural determination[44]. In the following, we will examine the elastic scattering cross-sections expressed without the pre-factors in Eq. (1), i.e. the structure factor,

$$\tilde{I}_{\tilde{\alpha}}(\mathbf{q}) = \left|\langle\phi_{\tilde{\alpha}}|\hat{L}\,|\phi_{\tilde{\alpha}}\rangle\right|^2 = |L_{\tilde{\alpha}\tilde{\alpha}}|^2, \tag{4}$$

such that $\tilde{I}$ is directly proportional to the elastic component of the total cross-section $(dS/d\Omega)$.

The molecular state $\tilde{\alpha}$ does not only depend on electronic coordinates, but also on the nuclear coordinates. Using the Born-Oppenheimer approximation and ignoring non-adiabatic couplings,

the total wavefunction for state $\tilde{\alpha}$ can be written as a direct product of rotational, vibrational and electronic wavefunctions,

$$\phi_{\tilde{\alpha}} = \Psi^{rot}_{JKM}(\Omega)\Psi^{vib}_{\nu}(\overline{\mathbf{R}})\Psi^{elec}_{\alpha}(\overline{\mathbf{r}};\overline{\mathbf{R}},\Omega), \tag{5}$$

where the electronic wavefunction, $\Psi^{elec}_{\alpha}(\overline{\mathbf{r}};\overline{\mathbf{R}},\Omega)$, depends parametrically on the nuclear coordinates $\overline{\mathbf{R}}$ and on the orientation of the molecular frame specified by the rotational angles $\Omega = (\theta,\phi,\chi)$. The rotational wavefunction $\Psi^{rot}_{JKM}(\Omega)$ is characterized by the three rotational quantum numbers J, K, and M, and the vibrational wavefunction $\Psi^{vib}_{\overline{\nu}}(\overline{\mathbf{R}})$ by the vibrational quantum numbers $\overline{\nu}$. Since the scattering operator in Eq. (2) only acts on the electrons, we first evaluate the scattering in terms of the fixed-nuclei form factor,

$$f^0_{\alpha}(\mathbf{q};\overline{\mathbf{R}},\Omega) = \langle\Psi^{elec}_{\alpha}|\hat{L}\,|\Psi^{elec}_{\alpha}\rangle = \int \rho_{\alpha}(\mathbf{r};\overline{\mathbf{R}},\Omega)\, e^{\imath\mathbf{qr}} d\mathbf{r}, \tag{6}$$

where evaluation of the bracket is equivalent to a Fourier transform of the electron density for electronic state α, $\rho_{\alpha}(\mathbf{r};\overline{\mathbf{R}},\Omega)$. The form factor $f^0_{\alpha}(\mathbf{q};\overline{\mathbf{R}},\Omega)$ can be calculated directly from the *ab initio* electronic wavefunction[28,31,45]. This can be done either via analytic Fourier transforms of the Gaussian primitives that constitute the *ab initio* electronic wavefunction, or via a numerical Fourier transform (FFT) of the electron density represented on a grid[28]. It is common in X-ray crystallography to approximate the electron density by a sum of spherical isolated atom densities, which gives rise to the independent atom model (IAM)[28,44].

Finally, the (proportional) molecular elastic scattering in Eq. (4), $\tilde{I}_{\tilde{\alpha}}(\mathbf{q})$, can be written as a convolution of $f^0_{\alpha}(\mathbf{q};\overline{\mathbf{R}},\Omega)$ over the probability distributions given by the rotational and vibrational wavefunctions,

$$\tilde{I}_{\tilde{\alpha}}(\mathbf{q}) = \left| \int |\Psi^{rot}_{JKM}(\Omega)|^2\, |\Psi^{vib}_{\overline{\nu}}(\overline{\mathbf{R}})|^2\, f^0_{\alpha}(\mathbf{q};\overline{\mathbf{R}},\Omega)\, d\overline{\mathbf{R}}\, d\Omega \right|^2. \tag{7}$$

For a diatomic, the rotational wavefunction is given by a spherical harmonic, $Y_{JM}(\theta,\phi)$, with $d\Omega = \sin\theta d\theta d\phi$, and the vibrational wavefunction $\Psi^{vib}_{\nu}(R)$ is specified by the internuclear distance R and a single vibrational quantum number ν.

As an aside, it is worth pointing out that for elastic scattering the above treatment is equivalent to a Fourier transform of the *total* electron density, accounting for nuclear degrees of freedom. For elastic scattering the scattering operator can be written in terms of the density operator,

$$\hat{L} = \int \hat{\rho}_{\mathrm{e}}(\mathbf{r}) e^{\imath\mathbf{qr}} d^3r \tag{8}$$

with the total electron density $\hat{\rho}_{\rm e}(\mathbf{r})$ given by the operator, $\hat{\rho}_{\rm e}(\mathbf{r}) = \sum_{j=1}^{N_{\rm e}} \delta(\mathbf{r} - \mathbf{r}_i)$. This formulation emphasizes that the elastic scattering occurs from the total electron density, giving an effective form factor $f_{\tilde{\alpha}}^0(\mathbf{q})$ that depends on the overall quantum state of the molecule. The advantage of this equivalent perspective is that it emphasizes that, for instance, the shape of the electron density of a diatomic molecule in the $J = 0$ rotational state is a spherical shell rather than a dumbbell.

III. COMPUTATIONAL

A. Electronic states and vibrational wavefunctions

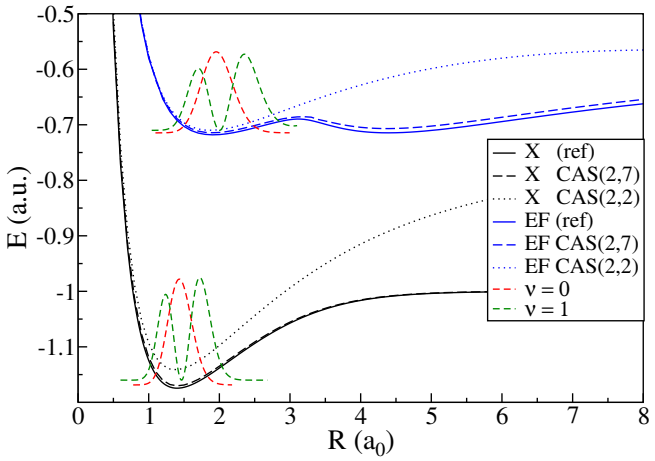

FIG. 1: Potential energy curves (PECs) for H_2 X and $EF\ ^1\Sigma_g^+$ states calculated at the CAS(2, 2)-SCF and CAS(2, 7)-SCF level of theory with basis sets aug-cc-pVTZ and aug-cc-pVQZ (results indistinguishable at the resolution of the figure). The reference PECs are taken from Wolniewicz[46,47]. The probability distributions for vibrational states $v = 0, 1$ are also included (arbitrary units).

We consider the ground $X^1\Sigma_g^+$ and first excited $EF^1\Sigma_g^+$ electronic states of H_2. The potential energy curves (PECs) for these states are calculated using multi-configurational Complete Active Space Self-Consistent Field theory at the CAS(2, 7)-SCF/aug-cc-pVQZ level using D_{2h} symmetry. The PECs are shown in Fig. 1 together with reference curves by Wolniewicz *et al.*[46,47]. A detailed comparison of the present calculations and the reference data at the stationary points is made in Table I. Overall, the present *ab-initio* calculations reproduce the reference curves well. The (2, 7) active space, with seven molecular orbitals (MOs) shown in Fig. 2, is necessary for a correct description at longer bond lengths, in particular to correctly predict the outer EF minimum, which requires additional bonding molecular orbitals such as $3A_g$, B_{2u} and B_{3u}, and for the ground-state at

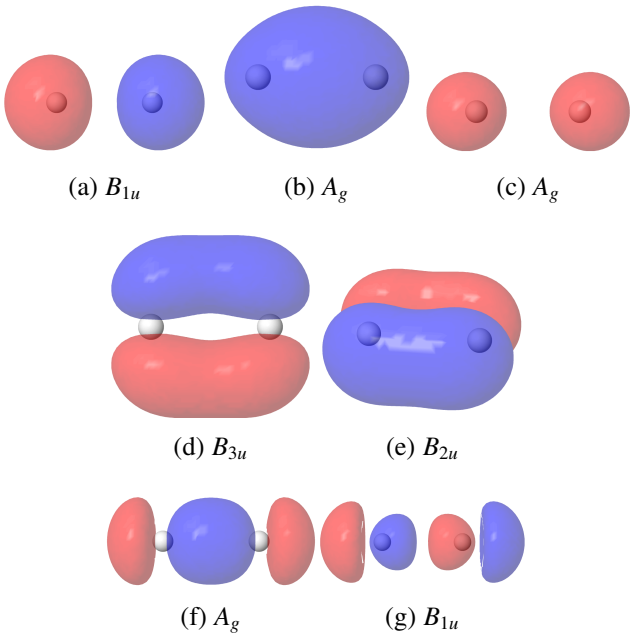

(a) B_{1u} (b) A_g (c) A_g

(d) B_{3u} (e) B_{2u}

(f) A_g (g) B_{1u}

FIG. 2: H_2 CAS(2, 7)-SCF/aug-cc-pVQZ active space molecular orbitals (MOs) with D_{2h} point group symmetry labels, at the outer EF minimum (R_F = 4.37475793 a_0). From left to right the molecular orbitals are ordered in terms of their energy.

Energy (E_h)	CAS(2, 7)	Reference	$\lvert E_{CAS} - E_{Ref} \rvert$
$U_X(R_0)$	-1.17089198	-1.17447311	0.00358113
$U_{EF}(R_E)$	-0.71554080	-0.71815235	0.00261155
$U_{EF}(R_F)$	-0.70762693	-0.71451800	0.00689107

TABLE I: H_2 *ab-initio* energies in atomic units calculated by CAS(2, 7)-SCF/aug-cc-pVQZ (present calculations) and reference values from Wolniewicz *et al.*[46,47]. The absolute energy difference between the two results is included in the third column. The comparison is done at the stationary points of the CAS(2, 7) potentials (see Fig. 1), at the ground state minimum, R_0 = 1.40493984 a_0, and at the inner and outer EF state minima, R_E = 1.90495263 a_0 and R_F = 4.37475793 a_0. The maximum difference in stationary point position between the CAS(2, 7)-SCF/aug-cc-pVQZ and the Wolniewicz calculations is $\triangle R$ = 0.016 a_0.

larger internuclear distances where for instance the B_{1u} σ^* MO contributes. The failure of a smaller (2, 2) active space at large R is demonstrated by the CAS(2, 2)-SCF PECs shown in Fig. 1. In the following, the Wolniewicz reference curves are used to calculate the vibrational wavefunctions, while the CAS-SCF *ab-initio* wavefunctions are used to calculate the electron density and the elastic X-ray scattering.

The vibrational wavefunctions are integrated using a 5*th* order Runge-Kutte algorithm, with the

orthonormality of the vibrational wavefunctions ensured via a Cholesky factorisation[48]. The calculation is done using the Wolniewicz reference PECs[46,47] and masses from the latest CODATA[49]. The vibrational probability distributions for the $v = 0, 1$ states on the X and EF potentials are shown in Fig. 1. The EF potential wells are less steep than the X state, leading to wider vibrational wavefunctions. The outer EF minimum supports two localized vibrational wavefunctions with $v = 0, 1$, with more excited vibrational wavefunctions spanning both EF minima[50].

B. AIXRD calculations

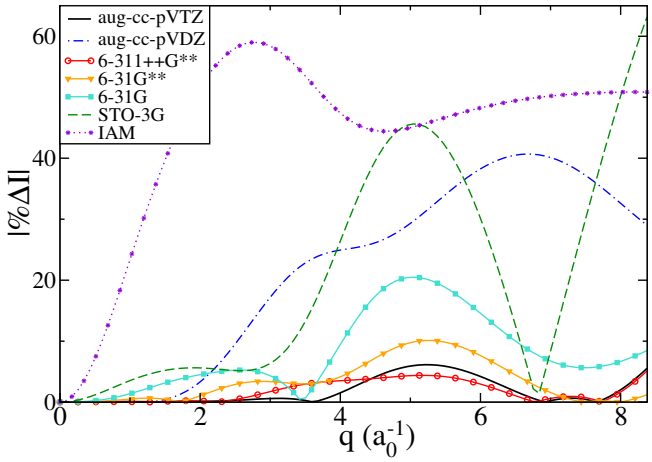

FIG. 3: Convergence of H_2 elastic scattering as a function of basis set shown in terms of $|\%\Delta\tilde{I}(q)|$ (see Eq. (9)), with CAS(2, 7)-SCF/aug-cc-pVQZ scattering calculations used as reference.

The elastic X-ray scattering is calculated directly from the electronic wavefunctions using the *ab-initio* X-ray diffraction (AIXRD) method presented in an earlier article[28]. This approach relies on analytical Fourier transforms of the Gaussian primitives that constitute the basis sets. Here, we examine the convergence of the elastic X-ray scattering signal as a function of the basis set and method for the H_2 molecule. The comparison is made in terms of the rotationally-averaged scattering, which produces radial curves that only depend on the momentum transfer q.

Fig. 3 shows the convergence of the X-ray elastic scattering for each method in terms of the absolute percent difference, $|\%\Delta\tilde{I}(q)|$, with the percent difference defined as,

$$\%\Delta\tilde{I}(q) = 100\frac{\tilde{I}_{\text{method}} - \tilde{I}_0}{\tilde{I}_0}, \tag{9}$$

where the reference scattering, $\tilde{I}_0$, is calculated using the CAS(2, 7)-SCF/aug-cc-pVQZ method.

METHOD	Error (%)		$\lvert E - E_{\mathrm{Ref}}\rvert$	Primitives		Speed-up
	Mean	Max	(10^{-2} E_h)	N_{g}	N_{gp}	
IAM	44.1	59.0	-	-		826.5
STO-3G	20.3	63.1	3.723	12	30	110.2
6-31G	7.9	20.5	2.819	16	56	59.0
6-31G**	3.4	10.1	1.011	28	90	36.7
6-311++G**	1.8	4.4	0.692	36	182	18.2
aug-cc-pVDZ	21.7	40.7	1.065	60	240	13.8
aug-cc-pVTZ	1.7	6.1	0.427	148	1122	3.0
aug-cc-pVQZ[a]	0.0	0.0	0.358	300	3306	1.0

[a] Used as reference

TABLE II: Comparison of accuracy and speed for various levels of theory for scattering from the $X^1\Sigma_g^+$ ground state at $R_0 = 1.40493984\ a_0$. The mean and maximum errors shown correspond to the errors in Fig. 3, with the scattering from CAS(2, 7)-SCF/aug-cc-pVQZ taken as reference (see Eq. (9)). The gap $|E - E_{\mathrm{ref}}|$ between calculated energies and Wolniewicz reference value[46] is used as a proxy for *ab-initio* convergence. The speed of the scattering calculations scales linearly with the number of non-zero unique Gaussian products per molecular orbital, N_{gp}, with the number of Gaussian primitives given by N_{g}. The IAM calculation uses tabulated atomic form factors[51].

All the listed *ab-initio* calculations are done at the CAS(2, 7)-SCF level, except for the STO-3G and 6-31G where CAS(2, 2)-SCF is used. The calculations are done for the $X^1\Sigma_g^+$ ground state at bond length $R_0 = 1.40493984\ a_0$, corresponding to the CAS(2, 7)-SCF/aug-cc-pVQZ $X^1\Sigma_g^+$ stationary point. In Table II the mean and the maximum absolute errors are given for each method. The mean absolute error is defined as,

$$\langle |\%\Delta\tilde{I}(q)| \rangle = \frac{1}{q_{max} - q_{min}} \int_{q_{min}}^{q_{max}} |\%\Delta\tilde{I}(q)|\, dq, \tag{10}$$

with integration over the interval $[q_{min}, q_{max}] = [0, 8.3]\ a_0^{-1}$. The method closest to the reference $\tilde{I}_0$ result is the calculation that uses the aug-cc-pVTZ basis, with a mean $\langle \%\Delta\tilde{I}(q) \rangle = 1.7\%$. The 6-311++G** calculation is a close second with $\langle \%\Delta\tilde{I}(q) \rangle = 1.8\%$. The poorest performing calculations are STO-3G, and somewhat surprising, the aug-cc-pVDZ. The comparative failure of STO-3G, 6-31G, and aug-cc-pVDZ at high q is likely to be due to a poor description of electron correlation and thus short-range features in the electron density.

The energy convergence of each *ab-initio* calculation relative the highly accurate Wolniewicz reference value[46], shown as $|E - E_{\mathrm{Ref}}|$ in Table II, predicts quite accurately the quality of the scattering AIXRD results. The energy convergence $|E - E_{\mathrm{Ref}}|$ ranks correctly the four best-performing methods, and identifies the three poorest performing ones. In terms of computational speed, also listed in Table II, the AIXRD calculations scale linearly with N_{gp}, which is the number of non-zero unique Gaussian products per molecular orbital. Note that $N_{\mathrm{gp}} < N_{\mathrm{g}}^2$, where N_{g} is the number of Gaussians primitives (in fact, $N_{\mathrm{gp}} \approx N_{\mathrm{g}}^{1.42}$ in the present set of calculations). In terms of a practical trade-off between accuracy and speed, AIXRD using the aug-cc-pVTZ basis performs almost as well as the quadruple-zeta basis set with mean $|\%\Delta I(q)|$=1.7 while being a factor three faster. The 6-311++G** basis provides an even better balance of speed and performance, with a factor 18 speed-up while maintaining a very low mean and maximum error, which might be of particular benefit for calculations in larger molecules.

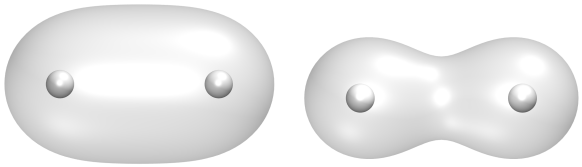

(a) *Ab-initio* (b) IAM

FIG. 4: Comparison of the electron densities implied by *ab-initio* calculations and the independent atom model (IAM). The electron density 87% isosurfaces are shown for ground-state H_2 at the equilibrium bond-length. Fig. 4a shows the results for CAS(2,7)-SCF/aug-cc-pVTZ, and Fig. 4b the corresponding IAM density.

The IAM method is also included in the comparisons presented in Fig. 3 and Table II. IAM is based on tabulated atomic form factors[51], and thus performs extremely well in terms of speed (> 800 speed-up), but rather poorly in terms of accuracy with a mean $\langle|\%\Delta I(q)|\rangle = 44.1\%$ deviation from the reference. All examined AIXRD methods are significantly more accurate than the IAM, especially in the important $q < 6\ a_0^{-1}$ range ($q < 12$ Å^{-1}), as can be seen in Fig. 3. This is due to a better overall description of the electron density compared to the IAM, which does not allow for any distortion of the electron density due to chemical bonding. The difference in electron density between *ab-initio* electronic structure calculations and IAM can be seen clearly in Fig. 4, which shows electron density isosurfaces for the H_2 ground-state. It is worth noting that the tabulated IAM form factors are taken from Hartree-Fock level *ab-initio* calculations[51].

IV. RESULTS

A. Scattering from specific electronic states

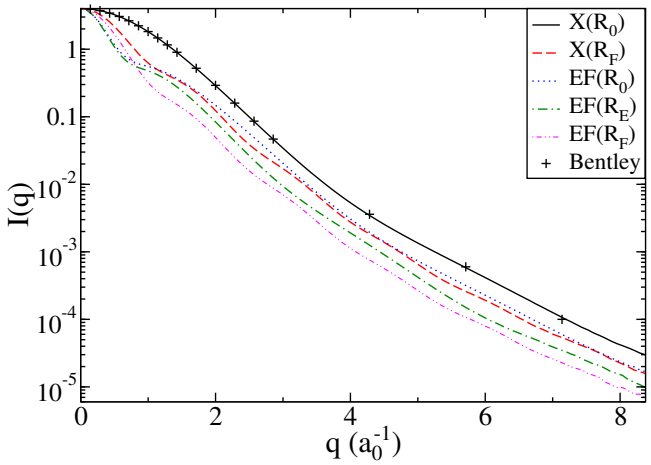

FIG. 5: Rotationally-averaged elastic X-ray scattering from the X and EF $^1\Sigma_g^+$ states in H_2, calculated at the ground-state equilibrium bond length, R_0, and at the EF inner and outer minima, R_E and R_F. The scattering is calculated at the CAS(2, 7)-SCF/aug-cc-pVTZ level. Previous calculations by Bentley and Stewart[31] are included for reference.

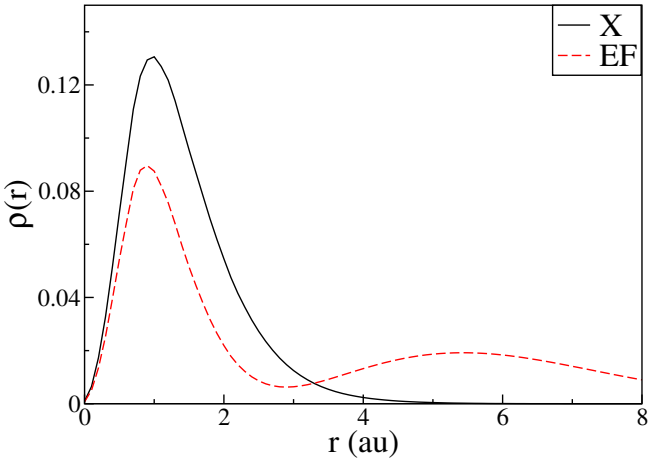

FIG. 6: Radially integrated electron density for the H_2 X and EF $^1\Sigma_g^+$ electronic states (calculated at the CAS(2, 7)-SCF/aug-cc-pVTZ level at internuclear distance R_0), with the radial distance r defined from the origin at the central point between the two nuclei.

We now consider the effect of different electronic states on the scattering. Figure 5 shows rotationally averaged elastic scattering curves for the X and EF electronic states of H_2 at three different bond lengths: the ground-state equilibrium bond length, R_0, and the EF inner and outer minima, R_E and R_F. The quality of the calculations is confirmed by comparison to previous scat-

tering curves calculated by Bentley and Stewart[31] which utilised a Davidson-Jones expansion of the essentially exact wavefunction for the H_2 ground-state at equilibrium geometry.

Each X-ray scattering curve is distinct, showing that not only changes in bond length alter the scattering but also changes in electronic structure. Vertical excitation from the ground X state to the EF state leads to a more diffuse electron density, with a corresponding drop in scattering intensity, in particular at small q ($q \in [0, 1]\ a_0^{-1}$) since small q's are sensitive to the overall size of the electron density, commensurate with the general principles of Fourier transforms. A second peak appears in the EF scattering at approximately $q = 1.5\ a_0^{-1}$, corresponding to a distance of approximately 4.2 a_0 in real space using the reciprocal relation $q = 2\pi/d$. Examination of the radially integrated electron density for the X and $EF\ ^1\Sigma_g^+$ electronic states for internuclear distance $R = R_0$, reveals that the electron density of the X ground-state decays smoothly, leading to an almost Gaussian scattering curve, while the EF electron density is concentrated in two shells, their centra separated roughly by 4 a_0, shown in Fig. 6. The main driver of this shift in electron density is a change of occupancy in the A_g orbitals. In the ground state, the first A_g MO (Fig. 2b) is highly occupied (occ=1.9634). After excitation, the second A_g MO (Fig. 2c) gains occupancy (occ=0.8183).

Changes in bond length also affect the scattering strongly, as can be seen by comparing the scattering curves for the EF state at bond lengths R_0 and R_E in Fig. 5, which are similar in shape but shifted in q. It is hard to separate the effect of the bond length from the effect of the electronic structure on the scattering, especially for a molecule like H_2 with no core electrons to balance the signal from the valence electrons. The difference between the scattering curves for $X(R_0 \rightarrow R_\mathrm{F})$ and $EF(R_\mathrm{E} \rightarrow R_\mathrm{F})$ is due to a combination of changes in bond length and the composition of the electronic wavefunction. For instance, at the inner EF minimum, R_E, the first two A_g orbitals are occupied (occ=1.1730 and occ=0.8175, respectively). These orbitals are almost Gaussian-like and encompass both nuclei evenly. At the outer minimum, R_F, the B_{1u} orbital which has a two-center character, becomes the most occupied (occ=1.0251 from occ=0.0075 at R_E). At the same time the second A_g orbital decreases in occupancy to occ=0.1094 and also acquires two-center character, while the first A_g orbital retains its smooth shape and a relatively large occupancy (occ=0.8324). There are other changes in occupancy, including that the more diffuse orbitals such as B_{2u} and B_{3u} gain about 1% of total occupancy. This means that going from R_E to R_F the electronic structure undergoes quite significant changes, making it difficult to decouple the effects of electronic structure and bond length.

B. Accounting for vibrations and rotations in scattering

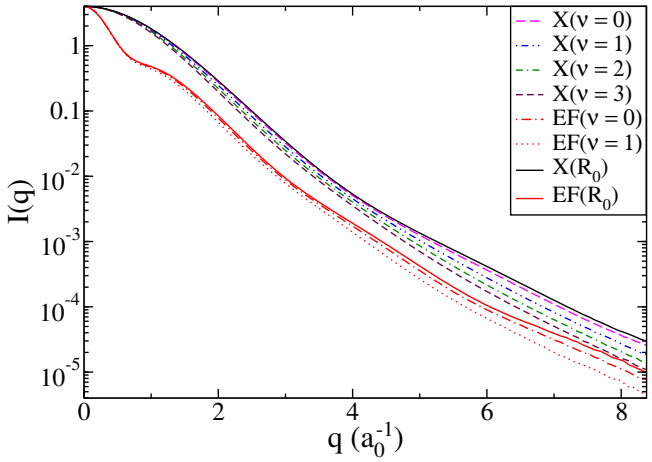

FIG. 7: H_2 $^1\Sigma_g^+$ $X(\nu = 0, 1, 2, 3)$ and $EF(\nu = 0, 1)$ rotationally averaged X-ray elastic scattering, with the scattering at fixed bond length R=R_0 included for reference. The scattering is calculated at the CAS(2, 7)-SCF/aug-cc-pVTZ level.

We begin by investigating the effect of vibrations on the scattering when rotational averaging is included. Rotationally averaged X-ray scattering curves are calculated from the H_2 $^1\Sigma_g^+$ $X(\nu = 0, 1, 2, 3)$ and $EF(\nu = 0, 1)$ states. These are shown in Fig. 7, which includes as reference the scattering from rigid $R = R_0$ molecules. It is clear that the electronic state change $X \rightarrow EF$ leaves a stronger signature in the scattering than the vibrational transitions, with the difference between vibrational states most noticable for high q (>3 a_0^{-1}). The difference in signal due to different vibrational states mostly relates to slight changes in the bond length distributions and thus in $\rho(\mathbf{r}; R)$. The $\nu = 0$ ground vibrational state scattering curves are very close to the rigid-molecule $R = R_0$ curves, since the ground vibrational state encompasses a rather narrow and nearly symmetric distribution about the equilibrium bond length R_0 (Fig. 1).

The difference between vibrational states becomes more apparent if the scattering signal is not rotationally averaged. Scattering from specific electronic, vibrational and rotational states ceases to be rotationally symmetric, such as the concentric rings in Fig. 11, and instead becomes a function of the scattering angles θ and ϕ, such as the images in Fig. 8. The radial scattering angle $\theta \in [0, \pi]$ relates to the amplitude of the momentum transfer vector as $|\mathbf{q}| = 2|\mathbf{k}_0| \sin(\theta/2)$. We focus on the selectively excited states reported in Ref.[23], which are $^1\Sigma_g^+$ $X(\nu = 1, J = 2, M = 0, 2)$. In the experiments, these states retained polarisation for >100 ns, which is sufficiently long for a hypothetical X-ray scattering experiment.

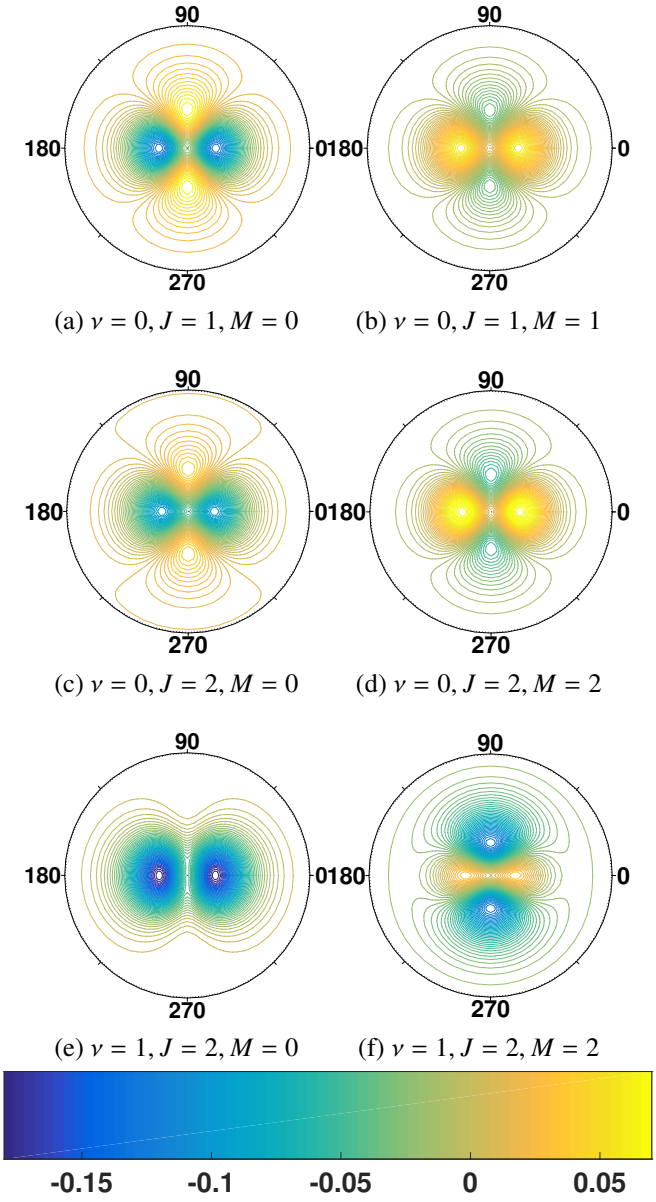

(a) $v = 0, J = 1, M = 0$ (b) $v = 0, J = 1, M = 1$

(c) $v = 0, J = 2, M = 0$ (d) $v = 0, J = 2, M = 2$

(e) $v = 1, J = 2, M = 0$ (f) $v = 1, J = 2, M = 2$

FIG. 8: Detector images for elastic scattering from H_2, calculated as the difference, $\Delta\tilde{I}(q) = \tilde{I}_{vJM}(q) - \tilde{I}_{000}(q)$, between specific rotational-vibrational states in the electronic ground-state and the reference rotational-vibrational ground-state ($v = 0, J = 0, M = 0$). The scattering is calculated at the CAS(2, 7)-SCF/aug-cc-pVTZ level for the electronic ground-state $X\ ^1\Sigma_g^+$. The $q_{max} = 1.4\ a_0^{-1}$ in the images and the X-rays are incident along the y-axis in the laboratory frame in which the rotational wavefunctions are defined.

Elastic scattering difference images for the (v=0,J=1,M=0,1), the (v=0,J=2,M=0,2), and the (v=1,J=2,M=0,2) are shown in Fig. 8, with the (v=0,J=0, M=0) electronic ground-state used as reference. The images are calculated such that the incoming X-rays align with the laboratory frame y-axis, with the rotational states defined relative the laboratory z-axis. The electronic orbitals were

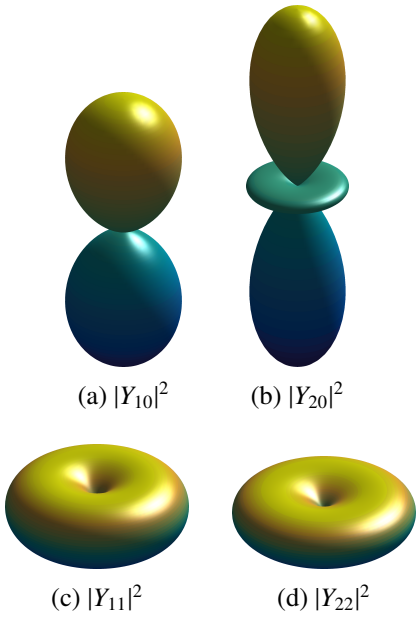

(a) $|Y_{10}|^2$ (b) $|Y_{20}|^2$

(c) $|Y_{11}|^2$ (d) $|Y_{22}|^2$

FIG. 9: Square-amplitude of the spherical harmonics, $|Y_{JM}(\theta, \phi)|^2$. The distance from the origin corresponds to the value of $|Y_{JM}(\theta, \phi)|^2$ in each direction - the colour and lighting are for aesthetic purposes only. The angle θ is defined relative the z-axis, which coincides with a C_∞ principal rotation axis, and the origin is a point of inversion.

inspected for consistency with the symmetry-restricted D_{2h} calculations used elsewhere in this article. The signal strengths shown in Fig. 8 correspond to percent differences relative the 000 ground state of between -45% and 50%, i.e. quite significant changes. The detector images are particularly apt at picking out changes in the rotational states, but also the vibrational states leave stronger signatures than in the rotationally averaged curves considered previously, as evident when comparing Fig. 8c and 8d, or 8e and 8f. The detector images for the $M = 0$ states are quite similar, irrespective of quantum number J (the v quantum number makes a bigger difference), as can be seen by comparing Fig. 8a and 8c. The same holds true for $|M| = J$ states, as can be seen by comparing Fig. 8b and 8d. This can be directly attributed to the overall shapes of the rotational wavefunctions, which are shown in Fig. 9. The $M = 0$ states have a dumbbell shape, while $|M| = J$ states are disc-shaped. Increasing J leads to a flatter disc, the effect of which is shown in Fig. 10 which compares the scattering patterns for (v=5,J=1,M=1) and (v=5,J=0,M=9). The higher angular momentum of the $J = 9$ state leads to a thinner disc, albeit this is limited by the intrinsic radius of the H-atoms. The choice of a high vibrational quantum number, $v = 5$ in this case, emphasizes the effect by increasing the radius of the disc.

Finally, it is worth noticing the importance of the direction of the incoming X-ray. As evident

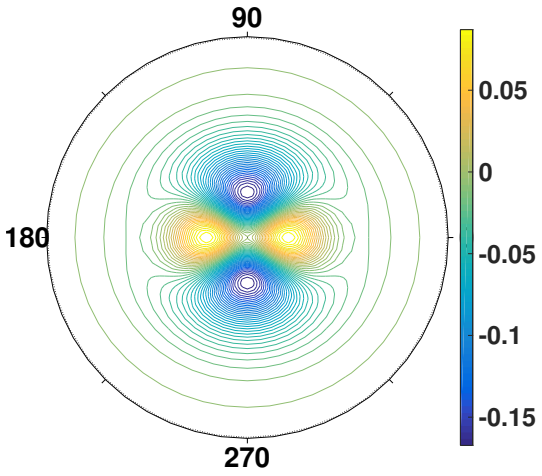

FIG. 10: Difference scattering image, $\triangle\tilde{I} = \tilde{I}_{511} - \tilde{I}_{599}$, for states ($v = 5, J = 1, M = 1$) and ($v = 5, J = 9, M = 9$). The difference in scattering reflects the gradual flattening of the rotational wavefunction, ultimately limited by the radius of the H-atoms.

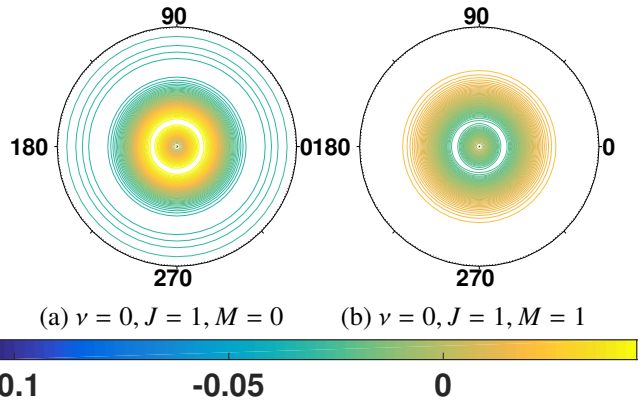

FIG. 11: Detector difference images calculated in the same manner as in Fig. 8, except that the X-rays are incident along the laboratory frame z-axis. In every other respect, the two figures above correspond to Figs. 8a-8b.

from Fig. 9, the square-amplitude of all spherical harmonics is symmetric around the z-axis. Figure 11 shows the scattering images that correspond to the images in Fig. 8a-8b when instead of being orthogonal to the z-axis, the incoming X-ray is parallel. The symmetry, or lack thereof, with respect of the X-ray is reflected in the scattering pattern.

C. Comparison to experiment

In a recent experiment, Liu *et al.* measured double differential cross-sections for H_2[13], providing an opportunity to compare the present calculations to experimental data obtained at the Taiwan

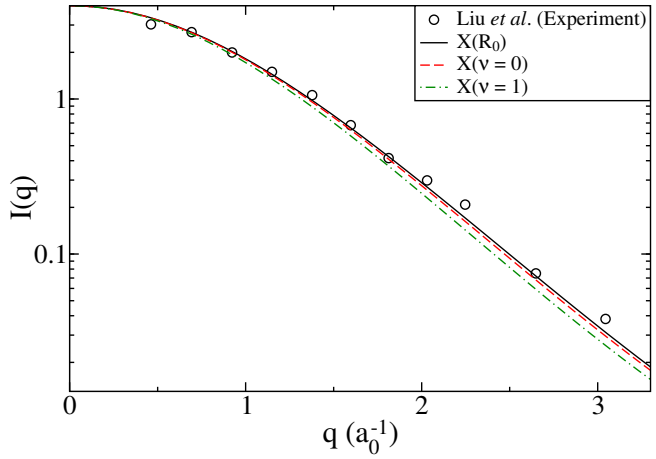

FIG. 12: Comparison to recent gas-phase H_2 X-ray scattering experiment. Elastic scattering data was obtained at the Taiwan Beamline BL12XU of SPring-8 with an incident photon energy of about 9889 eV and an energy resolution of about 70 meV[13]. The theoretical scattering curves are calculated using AIXRD as described in the present article, with wavefunctions calculated at the CAS(2, 7)-SCF/aug-cc-pVTZ level, both with the internuclear distance fixed at the equilibrium bond length, R_0, and for the $\nu = 0$ and $\nu = 1$ vibrational states.

Beamline BL12XU at SPring-8. Importantly, the experiment used an energy-resolved spectrometer with a resolution of about 70 meV to isolate the elastic signal, instead of recording the total signal which otherwise contains contributions from inelastic and even ionization channels.

The experimental results, together with theoretical AIXRD curves calculated at the equilibrium bond length R_0, as well as for H_2 vibrational states $\nu = 0$ and $\nu = 1$, are shown in Fig. 12. The curves shown have been rotationally averaged, as appropriate for a thermal 8.94 atm gas at equilibrium conditions. The R_0 and $\nu = 0$ curves are quite similar, as discussed previously, and it would require high resolution and very small errorbars on the experiment to distinguish them. The agreement between the calculated $\nu = 0$ curve and the experimental data validates our method for predicting molecular form factors based on *ab-initio* electronic structure calculations.

The scattering curve for the $\nu = 1$ vibrational state of H_2 is also included in the figure, but has extremely low population at room-temperature thermal conditions. The ratio of the $\nu = 0$ and $\nu = 1$ populations at $T = 298$ K is $N_0/N_1 = e^{-(E_0-E_1)/kT} \approx 1.6 \times 10^9$ according to the Boltzmann distribution, using $E_\nu = hc\tilde{\nu}(\nu + \frac{1}{2})$ with wavenumber $\tilde{\nu} = 4382.87$ cm^{-1} obtained from the CAS(2, 7)-SCF/aug-cc-pVTZ calculation (the experimental reference value is 4401.21 cm^{-1}[52]). However, it is apparent that for a non-negligible population of $\nu > 0$, it would become necessary to consider the excited vibrational state in the X-ray scattering, at least for high q.

V. DISCUSSION AND SUMMARY

The results in this article demonstrate that electronic structure leaves a strong signature in the elastic scattering signal, in particular for molecules with a large proportion of valence electrons as compared to core electrons. This is in agreement with previous work[28], with scattering from Rydberg states[27,53,54] constituting an extreme example. It is therefore important to account for electronic structure, and hence electron density, beyond the independent atom model (IAM) when considering electronically excited states, or even vibrationally excited states that protrude beyond any small region of the potential energy surface.

In the crystallography community, the shortcomings of IAM have been known for a long time. One of the first efforts to go beyond IAM was due to Stewart *et al.*[55], who used the hydrogen molecule to extract bound-hydrogen-atom form factors more suited for the refinement of high-resolution X-ray diffraction data obtained from organic molecular crystals. Stewart *et al.* then introduced generalized atomic form factors determined from a finite multipole expansion of the charge density about each nucleus[56,57], with the Fourier-Bessel coefficients of the pseudoatom radial density functions determined by a least-squares fit to the molecular form factor.

Although quite convenient, such pseudoatom approaches might be surpassed by the direct AIXRD approach[28]. Certainly, for excited electronic states that cannot be reduced to a small number of standard form factors, the AIXRD approach is by far the most effective and flexible. In this article, we have investigated the convergence properties of AIXRD and find that it scales linearly with the number of non-zero products of Gaussian primitives, N_{gp}, and that importantly, the quality of the wavefunction and thus the scattering correlates with the energy convergence, making it easy to assess the quality of the *ab-initio* scattering.

For vibrational states, we find that the signatures of specific states are strongest at large values of the momentum transfer q. Also, one must note that it is in general not possible to separate changes in scattering due to the bond length from changes due to the electronic structure. An interesting observation in our calculations is that if rotational states can be prepared selectively, this dramatically increases the information on the detector, not only in terms of identifying rotational states but also vibrational states. Recent state-selective experiments that achieve a high population transfer indicate that state-selective scattering might one day become experimental reality, especially if combined with the large photon-flux of XFEL sources.

The 'spectroscopic' techniques for state-selection are complemented by advances in molecular

alignment by highly focussed laser fields[58], which can be used to measure scattering form factors in the molecular frame. However, in contrast to the spectroscopic techniques, the strong-field methods excite rotational wavepackets or groups of states rather than single quantum states. Such dynamic control can be quite powerful[59–62], but may require further attention to the theoretical description of the scattering[63–65].

High-precision measurement of the differential cross section of X-ray elastic scattering from H_2[13] provides a welcome opportunity to examine molecular form factors and an interesting route for the study of the electronic structure of atoms and molecules. The excellent agreement between the experimental measurements and the calculations presented in this article hold promise that this approach could be extended to a wider range of molecules[28]. In the future, the prospect of identifying electronic states in conjunction with time-dependent ultrafast X-ray scattering could enable complete characterization of reaction paths using X-ray scattering. Recent time-resolved experiments[18–20,66] combined with theory[28,65,67] constitute an important first step towards this goal.

ACKNOWLEDGEMENTS

AK acknowledges funding from the European Union (FP7-PEOPLE-2013-CIG-NEWLIGHT) and the Leverhulme Trust (RPG-2013-365), as well as sabbatical support from the Wenner-Gren Foundations and the hospitality of Prof. Roland Lindh at Uppsala University.

REFERENCES

[1]P. Debye, L. Bewilogua, and F. Ehrhardt, *Zerstreuung von Röntgenstrahlen an einzelnen Molekülen (vorläufige Mitteilung)*, Phys. Zeits. **30**, 84 (1929).

[2]M. H. Pirenne, **The Diffraction of X-Rays and Electrons by Free Molecules** (Cambridge University Press: London, 1946).

[3]*The Scattering of X-Rays from Gases*, Phys. Rev. **32**, 22 (1928).

[4]E. O. Wollan, *Scattering of X-Rays from Gases*, Phys. Rev. **37**, 862 (1931).

[5]David R. Chipman and Laurence D. Jennings, *Measurement of the Atomic Scattering Factor of Ne, Ar, Kr, and Xe*, Phys. Rev. **132**, 728 (1963).

[6]I. Hargittai and M. Hargittai, **Stereochemical applications of gas-phase electron diffraction: Part A The Electron Diffraction Technique** (VCH, first edition, 1988).

[7]J. N. Galayda, J. Arthur, D. F. Ratner, and W. E. White, *X-ray free-electron lasers–present and future capabilities*, J. Opt. Soc. Am. B **27**, B106 (2010).

[8]Anton Barty, Jochen Kpper, and Henry N. Chapman, *Molecular Imaging Using X-Ray Free-Electron Lasers*, Ann. Rev. Phys. Chem. **64**, 415 (2013).

[9]C. Bostedt, J. D. Bozek, P. H. Bucksbaum, R. N. Coffee, J. B. Hastings, Z. Huang, R. W. Lee, S. Schorb, J. N. Corlett, P. Denes, P. Emma, R. W. Falcone, R. W. Schoenlein, G. Doumy, E. P. Kanter, B. Kraessig, S. Southworth, L. Young, L. Fang, M. Hoener, N. Berrah, C. Roedig, and L. F. DiMauro, *Ultra-fast and ultra-intense x-ray sciences: first results from the Linac Coherent Light Source free-electron laser*, J. Phys. B **46**, 164003 (2013).

[10]J. Feldhaus, M. Krikunova, M. Meyer, T. Möller, R. Moshammer, A. Rudenko, T. Tschentscher, and J. Ullrich, *AMO science at the FLASH and European XFEL free-electron laser facilities*, J. Phys. B **46**, 164002 (2013).

[11]M. Yabashi, H. Tanaka, T. Tanaka, H. Tomizawa, T. Togashi, M. Nagasono, T. Ishikawa, J. R. Harries, Y. Hikosaka, A. Hishikawa, K. Nagaya, N. Saito, E. Shigemasa, K. Yamanouchi, and K. Ueda, *Compact xfel and amo sciences: Sacla and scss*, J. Phys. B **46**, 164001 (2013).

[12]V. Lyamayev, Y. Ovcharenko, R. Katzy, M. Devetta, L. Bruder, A. LaForge, M. Mudrich, U. Person, F. Stienkemeier, M. Krikunova, T. Mller, P. Piseri, L. Avaldi, M. Coreno, P. OKeeffe, P. Bolognesi, M. Alagia, A. Kivimki, M. D. Fraia, N. B. Brauer, M. Drabbels, T. Mazza, S. Stranges, P. Finetti, C. Grazioli, O. Plekan, R. Richter, K. C. Prince, and C. Callegari, *A modular end-station for atomic, molecular, and cluster science at the low density matter beamline of FERMI@Elettra*, J. Phys. B **46**, 164007 (2013).

[13]Ya-Wei Liu, Xiao-Xun Mei, Xu Kang, Ke Yang, Wei-Qing Xu, Yi-Geng Peng, Nozomu Hiraoka, Ku-Ding Tsuei, Peng-Fei Zhang, and Lin-Fan Zhu, *Determination of the electronic structure of atoms and molecules in the ground state: Measurement of molecular hydrogen by high-resolution x-ray scattering*, Phys. Rev. A **89**, 014502 (2014).

[14]B.P. Xie, L.F. Zhu, K. Yang, B. Zhou, N. Hiraoka, Y.Q. Cai, Y. Yao, C.Q. Wu, E.L. Wang, and D.L. Feng, *Inelastic x-ray scattering study of the state-resolved differential cross section of compton excitations in helium atoms*, Phys. Rev. A **82**, 032501 (2010).

[15]L.F. Zhu, L.S. Wang, B.P. Xie, K. Yang, N. Hiraoka, Y.Q. Cai, and D.L. Feng, *Inelastic x-ray scattering study on the single excitations of helium*, J. Phys. B **44**, 025203 (2011).

[16]Y.-G. Peng, X. Kang, K. Yang, X.-L. Zhao, Y.-W. Liu, X.-X. Mei, W.-Q. Xu, N. Hiraoka, K.-D. Tsuei, and L.-F. Zhu, *Squared form factors of vibronic excitations in 1213.3 ev of nitrogen*

studied by high-resolution inelastic x-ray scattering, Phys. Rev. A **89** (2014).

[17]Jochen Küpper, Stephan Stern, Lotte Holmegaard, Frank Filsinger, Arnaud Rouzeée, Artem Rudenko, Per Johnsson, Andrew V. Martin, Marcus Adolph, Andrew Aquila, Sasa Bajt, Anton Barty, Christoph Bostedt, John Bozek, Carl Caleman, Ryan Coffee, Nicola Coppola, Tjark Delmas, Sascha Epp, Benjamin Erk, Lutz Foucar, Tais Gorkhover, Lars Gumprecht, Andreas Hartmann, Robert Hartmann, Guünter Hauser, Peter Holl, André Hömke, Nils Kimmel, Faton Krasniqi, Kai-Uwe Kühnel, Jochen Maurer, Marc Messerschmidt, Robert Moshammer, Christian Reich, Benedikt Rudek, Robin Santra, Ilme Schlichting, Carlo Schmidt, Sebastian Schorb, Joachim Schulz, Heike Soltau, John C. H. Spence, Dmitri Starodub, Lothar Strüder, Jan Thøgersen, Marc J. J. Vrakking, Georg Weidenspointner, Thomas A. White, Cornelia Wunderer, Gerard Meijer, Joachim Ullrich, Henrik Stapelfeldt, Daniel Rolles, and Henry N. Chapman, *X-Ray Diffraction from Isolated and Strongly Aligned Gas-Phase Molecules with a Free-Electron Laser*, Phys. Rev. Lett. **112**, 083002 (2014).

[18]Michael P. Minitti, James M. Budarz, Adam Kirrander, Joseph Robinson, Thomas J. Lane, Daniel Ratner, Kenichiro Saita, Thomas Northey, Brian Stankus, Vale Cofer-Shabica, Jerome Hastings, and Peter M. Weber, *Toward structural femtosecond chemical dynamics: imaging chemistry in space and time*, Faraday Discuss. **171**, 81 (2014).

[19]M. P. Minitti, J. M. Budarz, A. Kirrander, J. S. Robinson, D. Ratner, T. J. Lane, D. Zhu, J. M. Glownia, M. Kozina, H. T. Lemke, M. Sikorski, Y. Feng, S. Nelson, K. Saita, B. Stankus, T. Northey, J. B. Hastings, and P. M. Weber, *Imaging molecular motion: Femtosecond x-ray scattering of an electrocyclic chemical reaction*, Phys. Rev. Lett. **114**, 255501 (2015).

[20]J. M. Budarz, M. P. Minitti, D. V. Cofer-Shabica, B. Stankus, A. Kirrander, J. B. Hastings, and P. M. Weber, *Observation of Femtosecond Molecular Dynamics via Pumpprobe Gas Phase X-Ray Scattering*, J. Phys. B **49**, 034001 (2016).

[21]Brian Stankus, James M. Budarz, Adam Kirrander, David Rogers, Joseph Robinson, Thomas J. Lane, Daniel Ratner, Jerome Hastings, Michael P. Minitti, and Peter M. Weber, *Femtosecond Photodissociation Dynamics of Di-Iodobenzene by Gas-Phase X-ray Scattering and Photoelectron Spectroscopy*, Faraday Disc. **193**, xxx (2016).

[22]G.O. Sitz and R. L. Farrow, *Preparation and decay of alignment in n_2 ($v = 1$)*, J. Chem. Phys. **101**, 4682–4687 (1994).

[23]Nate C. M. Bartlett, Daniel J. Miller, Richard N. Zare, Dimitris Sofikitis, Peter T. Rakitzis, and Andrew J. Alexander, *Preparation of oriented and aligned H_2 and HD by stimulated raman*

pumping, J. Chem. Phys. **129**, 084312 (2008).

[24]N. Mukherjee, W. Dong, J.A. Harrison, and R.N. Zare, *Preparation of oriented and aligned H_2 and HD by stimulated raman pumping*, J. Chem. Phys. **138**, 051101 (2013).

[25]Nandini Mukherjee and Richard N. Zare, *Stark-induced adiabatic Raman passage for preparing polarized molecules*, J. Chem. Phys. **135** (2011).

[26]M. Ben-Nun, Todd J. Martinez, Peter M. Weber, and Kent R. Wilson, *Direct imaging of excited electronic states using diffraction techniques: theoretical considerations*, Chem. Phys. Lett. **262**, 405 (1996).

[27]A. Kirrander, *X-ray diffraction assisted spectroscopy of Rydberg states*, J. Chem. Phys. **137**, 154310 (2012).

[28]Thomas Northey, Nikola Zotev, and Adam Kirrander, *Ab Initio Calculation of Molecular Diffraction*, J. Chem. Theory Comput. **10**, 4911 (2014).

[29]Mark R. Pressprich, Mark A. White, and Philip Coppens, *Single-crystal x-ray analysis of an electronic excited state: the structure determination of a metastable state of sodium nitroprusside*, J. Am. Chem. Soc. **115**, 6444 (1993).

[30]Mark R. Pressprich, Mark A. White, Yanina Vekhter, and Philip Coppens, *Analysis of a metastable electronic excited state of sodium nitroprusside by x-ray crystallography*, J. Am. Chem. Soc. **116**, 5233 (1994).

[31]John Bentley and Robert F. Stewart, *Two-Center Calculations for X-Ray Scattering*, J. Comp. Phys. **11**, 127 (1973).

[32]Joseph D. Geiser and Peter M. Weber, *Pump-probe diffraction imaging of vibrational wave functions*, J. Chem. Phys. **108**, 8004 (1998).

[33]D. A. Kohl and E. J. Shipsey, *Elastic electron scattering from state-selected molecules I. Intensities*, Z. Phys. D **24**, 33 (1992).

[34]D. A. Kohl and E. J. Shipsey, *Elastic electron scattering from state-selected molecules II. Fourier transforms*, Z. Phys. D **24**, 39 (1992).

[35]N. Böwering, M. Volkmer, C. Meier, J. Lieschke, and M. Fink, *Electron diffraction from oriented molecules: e–CH_3CI*, Z. Phys. D **30**, 177 (1994).

[36]N. Böwering, M. Volkmer, Ch. Meier, J. Lieschke, and R. Dreier, *Electron diffraction from oriented molecules and implications for molecular structure analysis*, J. Molec. Struct. **348**, 49 (1995).

[37]Ryu Seol, Richard M. Stratt, and Peter M. Weber, *Diffraction Signals of Aligned Molecules in the Gas Phase: Tetrazine in Intense Laser Fields*, J. Phys. Chem. A **107**, 6622 (2003).

[38]Robin Santra, *Concepts in x-ray physics*, J. Phys. B **42**, 023001 (2009).

[39]A. Debnarova, S. Techert, and S. Schmatz, *Computational studies of the x-ray scattering properties of laser aligned stilbene*, J. Chem. Phys. **134**, 054302 (2011).

[40]Hensley Christopher, Jie Yang, and Martin Centurion, *Imaging of Isolated Molecules with Ultrafast Electron Pulses*, Phys. Rev. Lett. **109**, 133202 (2012).

[41]Winfried Schülke, **Electron Dynamics by Inelastic X-Ray Scattering** (Oxford Science Publications, first edition, 2007).

[42]I. Waller and D. R. Hartree, *On the Intensity of Total Scattering of X-Rays*, Proc. R. Soc. Lond. Ser.-A **124**, 119 (1929).

[43]L.S. Bartell and R.M. Gavin, *Effects of Electron Correlation in X-Ray and Eiectron Diffraction*, J. Am. Chem. Soc. **86**, 3493 (1964).

[44]Des McMorrow and Jens Als-Nielsen, **Elements of Modern X-Ray Physics** (Wiley-Blackwell, second edition, 2011).

[45]Andrea Debnarova and Simone Techert, *Ab initio treatment of time-resolved x-ray scattering: Application to the photoisomerization of stilbene*, J. Chem. Phys. **125**, 224101 (2006).

[46]L. Wolniewicz, *Nonadiabatic energies of the ground state of the hydrogen molecule*, J. Chem. Phys. **103**, 1792 (1995).

[47]T. Orlikowski, G. Staszewska, and L. Wolniewicz, *Long range adiabatic potentials and scattering lengths for the EF, e and h states of the hydrogen molecule*, Mol. Phys. **96**, 1445 (1999).

[48]A. R. Bainbridge, J. Harrington, A. Kirrander, C. Cacho, E. Springate, W. A. Bryan, and R. S. Minns, *VUV Excitation of a Vibrational Wavepacket in D_2 Measured through Strong-Field Dissociative Ionization*, New J. Phys. **17**, 103013 (2015).

[49]Peter J. Mohr, Barry N. Taylor, and David B. Newell, *CODATA Recommended Values of the Fundamental Physical Constants: 2010*, Rev. Mod. Phys. **84**, 1527 (2012).

[50]W. Kołos and L. Wolniewicz, *Theoretical investigation of the lowest double-minimum state $E,F^1\Sigma_g^+$ of the hydrogen molecule*, J. Chem. Phys. **50**, 3228 (1969).

[51]**International Tables for Crystallography Volume C: Mathematical, physical and chemical tables**, number ISBN 978-1-4020-1900-5 (Wiley, 2006 edition, 2006).

[52]Karl K. Irikura, *Experimental Vibrational Zero-Point Energies: Diatomic Molecules*, J. Phys. Chem. Ref. Data **36**, 2 (2007).

[53]Jeffrey L. Krause, Kenneth J. Schafer, M. Ben-Nun, and Kent R. Wilson, *Creating and Detecting Shaped Rydberg Wave Packets*, Phys. Rev. Lett. **79**, 4978 (1997).

[54]Henri J. Suominen and A. Kirrander, *How to observe coherent electron dynamics directly*, Phys. Rev. Lett. **112**, 043002 (2014).

[55]Robert F. Stewart, Ernest R. Davidson, and William T. Simpson, *Coherent X-Ray Scattering for the Hydrogen Atom in the Hydrogen Molecule*, J. Chem. Phys. **42**, 3175 (1965).

[56]Robert F. Stewart, John Bentley, and Bernard Goodman, *Generalized xray scattering factors in diatomic molecules*, J. Chem. Phys. **63**, 3786 (1975).

[57]John Bentley and Robert F. Stewart, *Diatomic Generalized X-Ray Scattering Factors: Results from HartreeFock Electron Density Functions*, J. Chem. Phys. **63**, 3794 (1975).

[58]H. Stapelfeldt and T. Seideman, *Colloquium: Aligning molecules with strong laser pulses*, Rev. Mod. Phys. **75**, 543 (2003).

[59]A. Kirrander and H. H. Fielding and Ch. Jungen, *Excitation, dynamics and control of rotationally autoionizing Rydberg states of H_2*, J. Chem. Phys. **127**, 164301 (2007).

[60]A. Kirrander and Ch. Jungen and H. H. Fielding, *Localization of electronic wave packets in H_2*, J. Phys. B **41**, 074022 (2008).

[61]A. Kirrander and H. H. Fielding and Ch. Jungen, *Optical phase and the ionization-dissociation dynamics of excited H_2*, J. Chem. Phys. **132**, 024313 (2010).

[62]A. Kirrander, Ch. Jungen, and H. H. Fielding, *Control of ionization and dissociation with optical pulse trains*, Phys. Chem. Chem. Phys. **12**, 8948 (2010).

[63]Ulf Lorenz, Klaus B. Møller, and Niels E. Henriksen, *Theory of time-resolved inelastic x-ray diffraction*, Phys. Rev. A **81**, 023422 (2010).

[64]Gopal Dixit, Oriol Vendrell, and Robin Santra, *Imaging electronic quantum motion with light*, Proc. Natl. Acad. Sci. **109**, 11636 (2012).

[65]Adam Kirrander, Kenichiro Saita, and Dmitrii V. Shalashilin, *Ultrafast X-ray Scattering from Molecules*, J. Chem. Theory Comput. **12**, 957 (2016).

[66]Christine C. Pemberton, Yao Zhang, Kenichiro Saita, Adam Kirrander, and Peter M. Weber, *From the (1B) Spectroscopic State to the Photochemical Product of the Ultrafast Ring-Opening of 1,3-Cyclohexadiene: A Spectral Observation of the Complete Reaction Path*, J. Phys. Chem. A **119**, 8832 (2015).

[67]A. Debnarova, S. Techert, and S. Schmatz, *Ab initio studies of ultrafast x-ray scattering of the photodissociation of iodine*, J. Chem. Phys. **133**, 124309 (2010).